JPE 15-5-13

http://dx.doi.org/10.6113/JPE.2015.15.5.1264
ISSN(Print): 1598-2092 / ISSN(Online): 2093-4718

Compensation of Periodic Magnetic Saturation Effects for the High-Speed Sensorless Control of PMSM Driven by Inverter Output Power Control-based PFC Strategy

Kwang-Woon Lee†

†Department of Electronic Engineering, Mokpo National Maritime University, Mokpo, Korea

Abstract

An inverter output power control based power factor correction (PFC) strategy is being extensively used for permanent magnet synchronous motor (PMSM) drives in appliances because such a strategy can considerably reduce the cost and size of the inverter. In this strategy, PFC circuits are removed and large electrolytic DC-link capacitors are replaced with small film capacitors. In this application, the PMSM *d-q* axes currents are controlled to produce ripples, the frequency of which is twice that of the AC main voltage, to obtain a high power factor at the AC mains. This process indicates that the PMSM operates under periodic magnetic saturation conditions. This paper proposes a back electromotive-force (back-EMF) estimator for the high-speed sensorless control of PMSM operating under periodic magnetic saturation conditions. The transfer function of the back-EMF estimator is analyzed to examine the effect of the periodic magnetic saturation on the accuracy of the estimated rotor position. A simple compensation method for the estimated position errors caused by the periodic magnetic saturation is also proposed in this paper. The effectiveness of the proposed method is experimentally verified with the use of a PMSM drive for a vacuum cleaner centrifugal fan, wherein the maximum operating speed reaches 30,000 rpm.

Key words: Back-EMF estimator, Inductance variation, Periodic magnetic saturation, Permanent-magnet synchronous motors (PMSMs), Sensorless control

I. INTRODUCTION

During the past decade, permanent magnet synchronous motors (PMSMs) have been extensively employed in appliances because of its higher efficiency compared to that of induction motors (IMs) [1]. Although IMs used in appliances do not require complex driving circuits, PMSM is often driven by a single-phase diode rectifier-fed inverter. Fig. 1(a) illustrates the general structure of the PMSM drive used in appliances. PMSM is driven by a single-phase diode rectifier-fed inverter, and the power factor correction (PFC) circuits are generally adopted to meet the IEC61000-3-2 harmonic current emission standard, wherein the limits on harmonic currents that can be allowed are listed [2]. The appliance industry is highly sensitive to cost competitiveness. An inverter output power control-based PFC strategy that involves removing the PFC circuits and replacing large electrolytic DC-link capacitors with a small film capacitor, as shown in Fig. 1(b), is currently gaining attention in the appliance industry because this strategy can significantly reduce the cost and size of the inverter [3]-[6]. Fig. 1(c) shows the experimental waveforms when the inverter output power control-based PFC strategy is employed for a PMSM drive. Fig. 1(c) also shows that the *q*-axis current is controlled to produce ripples with frequency that is twice that of the AC mains, indicating that the PMSM operates under periodic magnetic saturation conditions.

The PMSM position sensorless control is also an important issue in appliances because this control contributes in the cost reduction of the PMSM drive; the back electromotive-force

Manuscript received Feb. 12, 2015; accepted Apr. 26, 2015
Recommended for publication by Associate Editor Gaolin Wang.
†Corresponding Author: kwlee89@mmu.ac.kr
Tel: +82-61-240-7269, Fax: +82-61-240-7253, Mokpo Nat'l Maritime Univ.
Department of Electronic Engineering, Mokpo National Maritime University, Korea

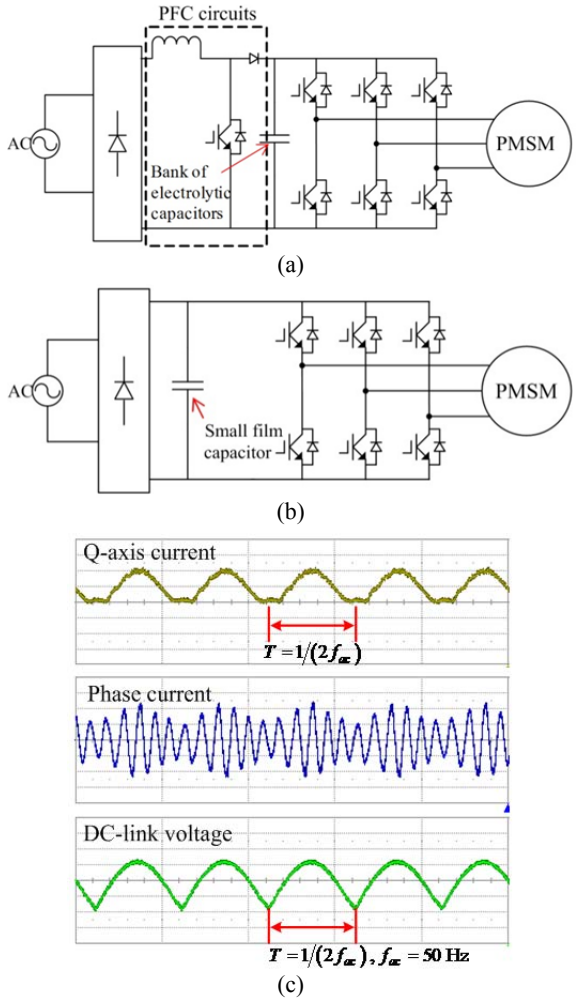

Fig. 1. (a) Configuration of a conventional PFC circuit-based PMSM drive. (b) Configuration of a single-phase diode rectifier-fed PMSM drive with a small DC-link capacitor. (c) Experimental waveforms of the *q*-axis current, phase current, and DC-link voltage when the inverter output power control-based PFC strategy is employed.

(back-EMF)-based sensorless control methods have also been commonly employed in appliances [7]. Numerous researches on the back-EMF based sensorless control of PMSM have been introduced [8]-[14]. The accuracy of the estimated back-EMF considerably depends on the model errors because the back-EMF is estimated on the basis of the PMSM mathematical model; thus, the performance of the sensorless controlled PMSM drive at high speeds is known to be highly sensitive to the *q*-axis inductance error [15]. When the inverter output power control-based PFC strategy is applied to the PMSM drive, the *d-q* axes inductances of PMSM also vary according to the periodic magnetic saturation. An online parameter estimation strategy can be considered to compensate for the effect of inductance variations caused by the periodic magnetic saturation on the estimated back-EMF. In [15], the online parameter estimation strategy is employed to estimate the value of the actual PMSM stator inductances during sensorless control; however, the use of online parameter estimation method increases the computation burden, and a zero-phase lag estimation of periodically varying parameters at twice the line frequency (at 100 Hz or 120 Hz) is a challenging task. A look-up table (LUT) saving the *d-q* axes inductance values based on the *d-q* axes currents can be considered to compensate for the periodically varying inductances. However, in view of the effects of dynamic inductance [16], the static inductance-based LUT clearly cannot completely compensate for the effects of periodic magnetic saturation in a sensorless controlled PMSM drive.

This paper proposes a high-speed sensorless control strategy for PMSM operating under periodic magnetic saturation conditions. The back-EMF estimator is implemented using a disturbance observer presented in [9], and the transfer function of the back-EMF estimator is analyzed in detail to examine the effect of stator inductance variations on the accuracy of the estimated back-EMF. Analysis shows that the estimated position error at high speeds mainly depends on the product of the *q*-axis inductance error and hypothetical *q*-axis current. The effect of periodic stator inductance variations on the estimated position error can be easily compensated by using a notch filter with a stop band of twice the line frequency (100 Hz or 120 Hz). The proposed method is applied to a PMSM installed in a vacuum cleaner centrifugal fan, wherein the maximum operating speed reaches 30,000 rpm. Experimental results are presented to verify the effectiveness of the proposed sensorless control method.

II. Power Factor Correction through Inverter Output Power Control

Assuming a unity power factor condition at the AC mains, the input power p_{in} at the AC mains is given as follows:

$$p_{in} = v_{pk} i_{pk} \sin^2 \theta_{grid} , \tag{1}$$

where v_{pk} and i_{pk} are the peak values of the AC mains voltage and current, respectively; θ_{grid} is the phase angle of the AC mains voltage; and θ_{grid} can be sensed from the AC mains voltage using an additional hardware or can be estimated from the DC-link voltage ripples [3]. In the same condition, the DC-link capacitor power p_c can be calculated as follows [4]:

$$p_c = \frac{1}{2} \omega_{in} C_{dc} v_{pk}^2 \sin\left(2\theta_{grid}\right), \tag{2}$$

where ω_{in} is the angular frequency of the mains voltage and C_{dc} denotes the capacitance of the DC-link capacitor.

The output power of the inverter p_{out} is given as follows:

$$p_{out} = \frac{3}{2}\left(v_d i_d + v_q i_q\right), \tag{3}$$

where v_d, v_q and i_d, i_q are the *d-q* axes stator voltages and currents, respectively, in the rotating reference frame.

Assuming that the the motor drive losses, including a single-phase diode rectifier, DC-link capacitors, and a

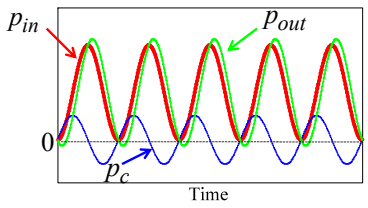

Fig. 2. Relationship among the input power, output power, and DC-link capacitor power under a unity power factor condition.

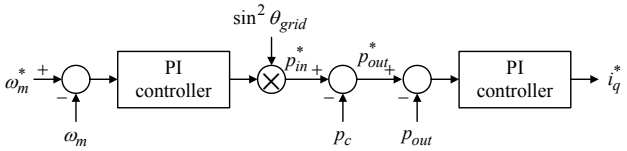

Fig. 3. Detailed structure of a speed controller to achieve a high power factor at the AC mains [4].

three-phase inverter, are negligible, p_{in} is equal to the sum of p_c and p_{out}. p_{in} and p_c for a unity power factor condition are given by (1) and (2), respectively; thus, a high power factor at the AC mains can be obtained by controlling p_{out} to exactly follow the reference given by

$$p_{out}^* = p_{in}^* - p_c \,, \tag{4}$$

where the superscript "*" denotes the reference value in each variable. Fig. 2 illustrates the relationship among p_{in} , p_c, and p_{out} under a unity power factor condition when the inverter output power control strategy given by (4) is employed. When the power factor is controlled this way, conventional PFC circuits are removed and large electrolytic DC-link capacitors are replaced with a small film capacitor; thus the size and cost of the inverter can be significantly reduced compared to the conventional PFC circuit-based inverter [5], [6].

Various control strategies have been introduced in [3–6] to obtain a high power factor at the AC mains through the inverter output power control. In this study, the *d-q* axes current command generation method presented in [4] was utilized. Fig. 3 shows that in the speed controller, the proportional-integral (PI) controller on the left-hand side outputs a control signal to regulate the rotor angular velocity. Thereafter, the control signal is multiplied by $\sin^2\theta_{grid}$ to generate the reference of the input power p^*_{in} for a unity power factor at the AC mains. The inverter output power reference p^*_{out} is obtained by subtracting p_c, which was calculated using (2), from p^*_{in}. The PI controller on the right-hand side of Fig. 3 outputs the *q*-axis current command to regulate the p_{out}, obtained using (3), to follow p^*_{out}. However, the *d*-axis current should also be appropriately controlled to obtain the aforementioned control object. The procedure for the generation of the *d*-axis current reference has been introduced in [4, 6], and the resulting *d*-axis current command is given by

$$i_d^* = -k_1\omega_m + k_2\omega_m \sin(2\omega_{in}t) \,, \tag{5}$$

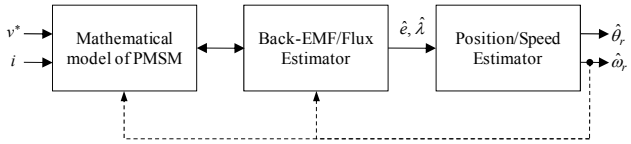

Fig. 4. Functional block diagram of the model-based sensorless control strategy [15].

where k_1 and k_2 are the gains used in adjusting the power factor at the AC-mains, and are selected through experiments or offline calculations; and ω_m is the mechanical rotor angular velocity.

Fig. 2 shows that the drawback of the PFC method through the inverter output power control is that torque ripples, the frequency of which is twice that of the AC mains voltage, are generated because of the ripples in the inverter output power. Cost competitiveness is a highly critical issue in the appliance industry; thus, the torque ripples caused by the PFC control can be allowed if the entire performance of the PMSM drive shown in Fig. 1(b) is still better than that of IM. For example, Fig. 2 shows that the inverter output power ripples exert limited effects on the noise level of a vacuum cleaner. However, the periodically varying *d-q* axes stator currents resulting from the inverter output power ripples cause the variation of the stator inductance with the same frequency. Therefore, an in-depth study on the high-speed sensorless control for this application is required because parameter errors caused by magnetic saturation degrade the performance of the sensorless position estimator [15].

III. Proposed Back-EMF Estimator for the High-Speed Sensorless Control of PMSM Operating under Periodic Magnetic Saturation Conditions

A. Selection of Sensorless Control Strategy Considering Periodic Magnetic Saturation Effects

Various model-based sensorless control strategies for PMSM have been proposed [7]-[14]; however, Fig. 4 shows that most of these strategies have a common functional block diagram [17]. The back-EMF or flux is estimated using the voltage commands v^*, the measured stator currents i, the PMSM mathematical model, and the rotor position and speed are obtained from the estimated back-EMF($\hat{e}$) or flux($\hat{\lambda}$) using an additional position/speed estimator.

The operating characteristics of the model-based sensorless position/speed estimator is significantly affected by the type of PMSM mathematical model used in the back-EMF or flux estimator. The PMSM voltage equation in the stationary reference frame is given by

$$\begin{bmatrix} v_\alpha \\ v_\beta \end{bmatrix} = \begin{bmatrix} R_s + pL_d & \omega_r\left(L_d - L_q\right) \\ -\omega_r\left(L_d - L_q\right) & R_s + pL_d \end{bmatrix} \begin{bmatrix} i_\alpha \\ i_\beta \end{bmatrix} + E_{ex} \begin{bmatrix} -\sin\theta_r \\ \cos\theta_r \end{bmatrix} \tag{6}$$

$$E_{ex} = \omega_r\left[\left(L_d - L_q\right)i_d + \lambda_{PM}\right] - \left(L_d - L_q\right)\left(pi_q\right), \tag{7}$$

where v_α, v_β and i_α, i_β are stator voltages and currents,

respectively, in the stationary reference frame: R_s is a stator resistance; L_d and L_q are *d-q* axes stator inductances; p is a differential operator; ω_r and θ_r are an electrical rotor angular velocity and position, respectively; λ_{PM} is a permanent magnet flux linkage; and E_{ex} is the extended EMF introduced in [8].

The second term on the right-hand side of (6) represents the back-EMFs; the rotor position can be directly acquired from the back-EMFs when using the stationary reference frame model. Note from (6) that the back-EMFs in the stationary reference frame are AC signals; thus, phase lagging exists between the actual and estimated back-EMFs caused by the intrinsic phase delay of the back-EMF estimator. This phase lagging increases as the rotor speed increases; thus, the performance of the sensorless control is often degraded at high speeds when using the stationary reference frame model-based back-EMF estimator [17].

The phase lagging problem at high speeds when using the stationary reference frame model-based sensorless control can be avoided by estimating the fluxes instead of the back-EMFs [14]. However, considering the specific application where PMSM operates under periodic magnetic saturation condition, the estimated flux signals are AC signals, the frequency of which varies based on the speed; the model errors resulting from the periodic magnetic saturation, caused by the inverter output power-based PFC control, have a frequency that is twice that of the AC mains voltage. Therefore, compensating for the effect of the periodic model errors on the estimated flux signals is difficult without affecting the phase angle of the estimated flux signals over extensive operating ranges. Nevertheless, the estimated back-EMFs become DC signals when using the rotating reference frame model based-back-EMF estimator; thus, separating the periodic magnetic saturation effect from the estimated back-EMFs is relatively easy. For this reason, the rotating reference frame model-based back-EMF estimator was employed in this study.

The PMSM voltage equation in the rotating reference frame is given as follows:

$$\begin{bmatrix} v_d \\ v_q \end{bmatrix} = \begin{bmatrix} R_s + pL_d & -\omega_r L_q \\ \omega_r L_q & R_s + pL_d \end{bmatrix} \begin{bmatrix} i_d \\ i_q \end{bmatrix} + E_{ex} \begin{bmatrix} 0 \\ 1 \end{bmatrix}. \tag{8}$$

By transforming (8) into the hypothetical rotating reference frame, which is the γ-δ reference frame presented in [11], the voltage equation of the PMSM can be expressed as follows:

$$\begin{bmatrix} v_\gamma \\ v_\delta \end{bmatrix} = \begin{bmatrix} R_s + pL_d & -\omega_r L_q \\ \omega_r L_q & R_s + pL_d \end{bmatrix} \begin{bmatrix} i_\gamma \\ i_\delta \end{bmatrix} + \begin{bmatrix} e_\gamma \\ e_\delta \end{bmatrix} + \left(\hat{\omega}_r - \omega_r\right) L_d \begin{bmatrix} -i_\delta \\ i_\gamma \end{bmatrix} \tag{9}$$

$$\begin{bmatrix} e_\gamma \\ e_\delta \end{bmatrix} = E_{ex} \begin{bmatrix} -\sin\Delta\theta \\ \cos\Delta\theta \end{bmatrix}, \tag{10}$$

where v_γ, v_δ and i_γ, i_δ are stator voltages and currents, respectively, in the γ-δ frame; $\Delta\theta$ is the angle difference between the *d-q* and the γ-δ reference frame, which represents the position error between the actual and hypothetical rotor positions; and $\hat{\omega}_r$ is the angular velocity of the rotating γ-δ frame. Equation (10) shows that the back-EMFs in the γ-δ reference frame are DC signals and contain the position error $\Delta\theta$; thus, the rotor speed and PMSM position can be estimated from the back-EMFs. When using the rotating reference frame model-based back-EMF estimator, the phase lagging between the actual and estimated back-EMFs becomes negligible at steady-states; thus, the rotating reference frame model of PMSM is often preferred for the high-speed sensorless control [11]. The drawback of the rotating reference frame model-based back-EMF estimator is that the estimated speed is used for estimating back-EMFs; thus, the performance of the back-EMF estimator can be degraded by the estimated speed error, particularly at low speeds. However, the effect of the speed estimation error on the estimated back-EMFs decreases as the speed increases when considering the synchronous operation of PMSM and the low-pass filtering effect caused by the mechanical system inertia.

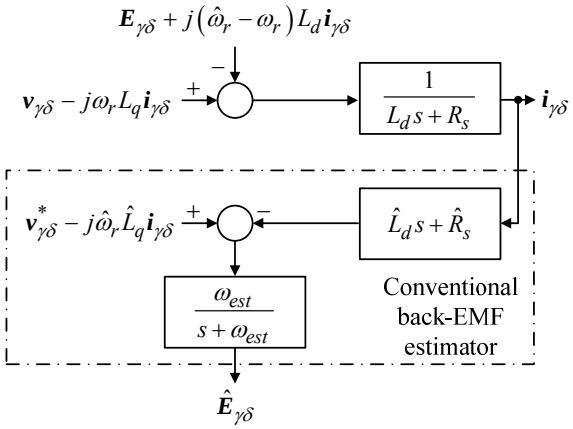

Fig. 5. Structure of the back-EMF estimator [9].

B. Back-EMF-based Sensorless Speed/Position Estimator in the Rotating Reference Frame

To estimate the back-EMF using the rotation reference frame model of PMSM, the disturbance observer-based back-EMF estimator, presented in [9], was employed because the overall structure of the estimator is simple and easy to implement. Fig. 5 illustrates the entire structure of the back-EMF estimator. Fig. 5 also shows that $\hat{R}_s$, $\hat{L}_d$, and $\hat{L}q$ represent the nominal values of the stator resistance and *d-q* axes stator inductances, respectively; ω_{est} denotes the bandwidth of the first-order low-pass filter; j is the imaginary unit ($=\sqrt{-1}$); and $\boldsymbol{v}_{\gamma\delta}$, $\boldsymbol{i}_{\gamma\delta}$, and $\hat{\boldsymbol{E}}_{\gamma\delta}$ are the vector representations of the stator voltages, stator currents, and estimated back-EMFs in the γ-δ reference frame, respectively.

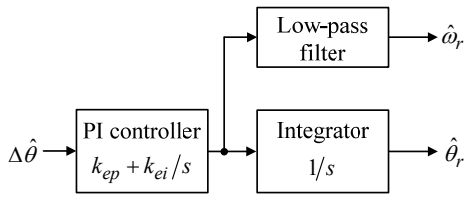

Fig. 6. Structure of the PLL type speed/position estimator [9].

Therefore, $\boldsymbol{v}_{\gamma\delta} = v_\gamma + jv_\delta$, $\boldsymbol{i}_{\gamma\delta} = i_\gamma + ji_\delta$, and $\hat{\boldsymbol{E}}_{\gamma\delta} = \hat{e}_\gamma + j\hat{e}_\delta$.

The estimated rotor position error $\Delta\hat{\theta}$ can be obtained from the estimated back-EMFs as follows:

$$\Delta\hat{\theta} = \tan^{-1}\left(\frac{-\hat{e}_\gamma}{\hat{e}_\delta}\right), \tag{11}$$

where $\hat{e}_\gamma$ and $\hat{e}_\delta$ are the estimated back-EMFs in the γ-δ reference frame. Fig. 6 shows that the estimated rotor speed () and position $\hat{\omega}_r$ $\hat{\theta}_r$ () are obtained from $\Delta\hat{\theta}$ using the phase-locked loop (PLL) type estimator.

C. Analysis of the Effect of Model Parameter Errors on the Estimated Back-EMF and Position Errors [17, 18]

Fig. 5 shows that the expression of the estimated back-EMF is obtained as follows:

$$\hat{\boldsymbol{E}}_{\gamma\delta} = \frac{\omega_{est}}{s+\omega_{est}}\left\{\boldsymbol{v}^*_{\gamma\delta} - j\hat{\omega}_r\hat{L}_q\boldsymbol{i}_{\gamma\delta} - \left(\hat{L}_d s + \hat{R}\right)\boldsymbol{i}_{\gamma\delta}\right\}. \tag{12}$$

From (9), $\boldsymbol{i}_{\gamma\delta}$ can be derived as

$$\boldsymbol{i}_{\gamma\delta} = \frac{\boldsymbol{v}_{\gamma\delta} - \boldsymbol{E}_{\gamma\delta} - j\left[\left(\hat{\omega}_r - \omega_r\right)L_d + \omega_r L_q\right]\boldsymbol{i}_{\gamma\delta}}{L_d s + R_s}. \tag{13}$$

From (12) and (13), $\hat{\boldsymbol{E}}_{\gamma\delta}$ can be expressed as

$$\hat{\boldsymbol{E}}_{\gamma\delta} = \frac{\omega_{est}}{s+\omega_{est}}\left\{\frac{\hat{L}_d s + \hat{R}_s}{L_d s + R_s}\left[\boldsymbol{E}_{\gamma\delta} - \boldsymbol{v}_{\gamma\delta} + j\left(\left(\hat{\omega}_r - \omega_r\right)L_d + \omega_r L_q\right)\boldsymbol{i}_{\gamma\delta}\right] + \boldsymbol{v}^*_{\gamma\delta} - j\hat{\omega}_r\hat{L}_q\boldsymbol{i}_{\gamma\delta}\right\}. \tag{14}$$

Under steady-state and high-speed conditions, it assumed that $\hat{\omega}_r$ is almost the same as ω_r because of the synchronous operation of PMSM. The voltage error between $\boldsymbol{v}^*_{\gamma\delta}$ and $\boldsymbol{v}_{\gamma\delta}$ primarily originates from the nonlinearity of the inverter caused by the dead-time; the relative magnitude of the voltage error caused by the dead-time to the inverter output voltage is known to decreas as the speed increases [19]. The stator resistance linearly varies based on temperature, and the relative magnitude of the voltage drop at the stator resistance to the inverter output voltage also decreases as the speed increases [19]. Therefore, when PMSM runs at high-speeds, the effect of the voltage error caused by the dead-time and the stator resistance variation on the estimated back-EMF can be ignored. From these assumptions, $\hat{\boldsymbol{E}}_{\gamma\delta}$ in (14) can be expressed as follows:

$$\hat{\boldsymbol{E}}_{\gamma\delta} = \frac{\omega_{est}}{s+\omega_{est}}\left\{\left(1 - \frac{\Delta L_d s}{L_d s + R_s}\right)\boldsymbol{E}_{\gamma\delta} + \frac{\Delta L_d s}{L_d s + R_s}\boldsymbol{v}_{\gamma\delta} - j\frac{\omega_r L_q \Delta L_d s}{L_d s + R_s}\boldsymbol{i}_{\gamma\delta} + j\omega_r\Delta L_q\boldsymbol{i}_{\gamma\delta}\right\}, \tag{15}$$

where ΔL_d and ΔL_q denote the error between the actual and nominal values, respectively, of the stator inductance; $\Delta L_d = L_d - \hat{L}_d$ thus,, $\Delta L_q = L_q - \hat{L}_q$.

The term $s/(L_d s+R_s)$ included in (15) is a first-order high-pass filter. From (15), the high-pass filter outputs are observed to be fed into the loss-pass filter $\omega_{est}/(s+\omega_{est})$; thus, the effect of the high-pass filtered terms in (15) on $\hat{\boldsymbol{E}}_{\gamma\delta}$ can be ignored when the cut-off frequency of the high-pass filter is higher than that of the low-pass filter. The *d*-axis inductance variation caused by the magnetic saturation is also relatively low compared to the *q*-axis inductance variation [20]. Therefore, (15) can be simplified as follows:

$$\hat{\boldsymbol{E}}_{\gamma\delta} \approx \frac{\omega_{est}}{s+\omega_{est}}\left\{\boldsymbol{E}_{\gamma\delta} + j\omega_r\Delta L_q\boldsymbol{i}_{\gamma\delta}\right\}. \tag{16}$$

From (11) and (16), $\Delta\hat{\theta}$ is given by

$$\Delta\hat{\theta} = \tan^{-1}\left(\frac{E_{ex}\sin\Delta\theta + \omega_r\Delta L_q i_\delta}{E_{ex}\cos\Delta\theta - \omega_r\Delta L_q i_\gamma}\right). \tag{17}$$

Fig. 6 shows that the role of the PLL-type speed/position estimator is to regulate $\Delta\hat{\theta}$ to be zero; thus, $\Delta\theta$ at the steady-state conditions can be derived from (17) as follows:

$$\Delta\theta = \sin^{-1}\left(\frac{-\omega_r\Delta L_q i_\delta}{E_{ex}}\right) = \sin^{-1}\left[\frac{-\Delta L_q i_\delta}{\left(L_d - L_q\right)\left(i_d - pi_q/\omega_r\right) + \lambda_{PM}}\right]. \tag{18}$$

To confirm the validity of (18), simulations using the PMSM parameters listed in Table I were performed. The effect of ΔL_q on $\Delta\theta$ was examined from the simulation results, and $\Delta\theta$ calculated from (18), wherein i_δ and i_d are obtained from the simulation results, was compared with the value measured from the simulation results. In the simulation, the inverter DC-link voltage was set to 300 V, which means that the inverter output power control-based PFC strategy is not employed in the simulation. The reference speed was set to 30,000 rpm, the PWM frequency was set to 15 kHz, and the bandwidth of the back-EMF estimator ω_{est} was set to 100 Hz. Fig. 7 illustrates the *d*-*q* axes inductance variation of PMSM used in this study based on the magnetic saturation. Fig. 7 also shows that L_q decreases by up to 30% from its maximum value as the stator of the PMSM is saturated. This result was reflected in the simulations.

TABLE I
PMSM NOMINAL PARAMETERS

Parameter	Value [unit]
Maximum speed	33,000 [rpm]
Stator resistance	0.526 [Ω]
D-axis inductance	3.97 [mH]
Q-axis inductance	6.0 [mH]
PM flux linkage	0.0226 [Wb]
Number of poles	2

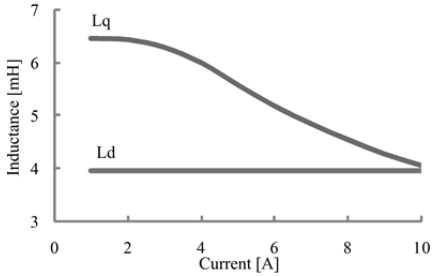

Fig. 7. The *d-q* axes stator inductance variation based on the magnetic saturation.

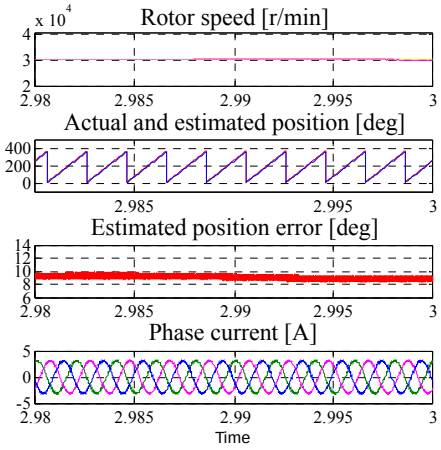

(a)

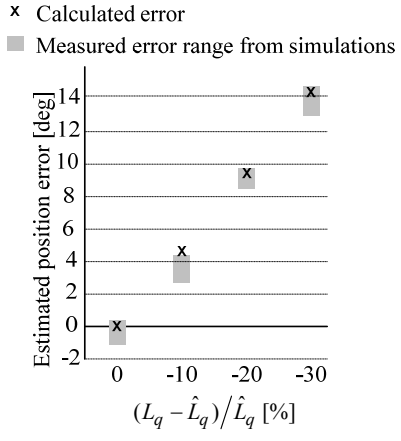

(b)

Fig. 8. (a) Simulation result for the sensorless control of PMSM under L_q error condition. (b) Comparison between the measured and calculated estimated position errors.

Fig. 8 illustrates one case from the simulation results for the high-speed sensorless control of PMSM, where $\hat{L}_q$ is set to 6.0 mH and L_q is set to 20% less than $\hat{L}_q$; and a comparison result between the measured $\Delta\theta$ from the simulation results and the calculated $\Delta\theta$ from (18). Fig. 8(a) shows that the estimated position error ranges between 8.5 and 9.7 degrees. By comparing Fig. 8(a) with Fig. 8(b), note that the analysis of $\Delta\theta$, given by (18), shows a satisfactory accuracy.

D. Proposed Back-EMF Estimator Considering Periodic Magnetic Saturation Effects

When the PFC function is performed by the strategy presented in Section II, i_q (or i_δ) has the ripples, the frequency of which is twice that of the AC mains, which is $2\omega_{in}$. From (18), the effect of pi_q on $\Delta\theta$ clearly becomes small as ω_r increases; therefore, $\Delta\theta$ at high-speeds primarily depends on $\Delta L_q i_\delta$, and has ripples with the same frequency as $2\omega_{in}$. As analyzed in (15) and (16), the back-EMF estimator, which is shown in Fig. 5, acts as a low-pass filter with a cut-off frequency at ω_{est}. Therefore, the ripples of $\Delta L_q i_\delta$ are not filtered out through the back-EMF estimator, and exert a direct influence on $\Delta\theta$. An exact zero-phase lag estimation of L_q is required to compensate for the effect of $\Delta L_q i_\delta$ on $\Delta\theta$. However, these types of application would encounter difficulty, wherein the *d-q* axes currents and voltages have ripples with frequency of $2\omega_{in}$. To cope with this problem, this study proposes a simple method, in which a notch filter is added to the back-EMF estimator to filter out the signals with frequency of $2\omega_{in}$. Fig. 9(a) illustrates the general block diagram of the proposed back-EMF estimator. Fig. 9(a) shows that the cut-off frequency of the notch filter is determined by ω_n, which is set to have the same frequency as $2\omega_{in}$. Figure 9(b) illustrates the bode plots of the conventional and the proposed back-EMF estimators, shown in Figs. 5 and 9(a), respectively, where no parameter errors are assumed; and ζ, ω_n, and ω_{est} were set to 0.7, 100 Hz, and 100 Hz, respectively. Fig. 9(b) shows that the ripples with frequency of 100 Hz would be filtered out through the proposed back-EMF estimator; however, phase lagging is slightly increased at low-frequencies. The phase lagging can degrade the back-EMF estimator performance at transient states; however, this performance degradation caused by the slight increase in phase lagging is negligible for this application because the target application of the proposed back-EMF estimator is a vacuum cleaner, which mainly operates at steady states. The effectiveness of the proposed method will be demonstrated through experiments.

IV. EXPERIMENTAL RESULTS

Experiments were conducted using a vacuum cleaner centrifugal fan to prove the validity of the proposed

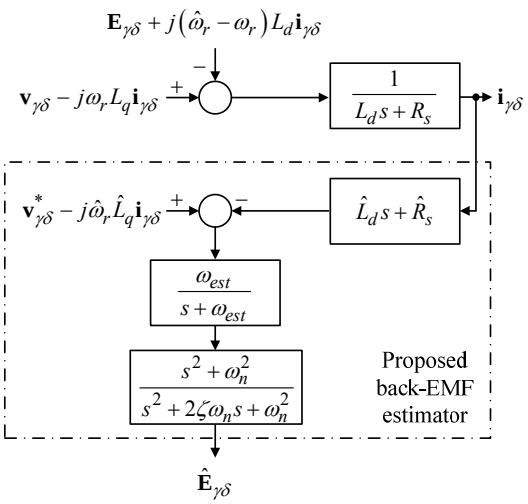

(a)

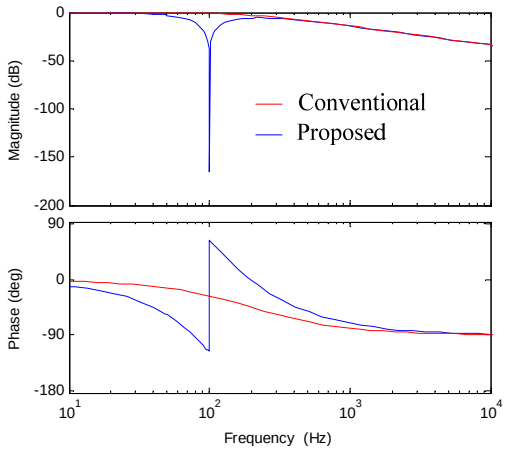

(b)

Fig. 9. (a) Structure of the proposed back-EMF estimator. (b) Bode plots of the conventional and the proposed back-EMF estimator.

back-EMF estimator for the high-speed sensorless control of PMSM operating under periodic magnetic saturation conditions. Figure 10 illustrates the experimental setup, wherein the vacuum cleaner centrifugal fan is installed into a box to shelter the noise of the fan during the experiments. The RMS voltage and the frequency of the AC mains are set to 230 V and 50 Hz, respectively. The parameters and the *d-q* axes stator inductances based on the PMSM magnetic saturation are the same as those in Table I and Fig. 7, respectively. The PMSM load condition is the same as that of a typical fan because PMSM was installed in a vacuum cleaner fan. The rated speed and torque of PMSM are 30,000 rpm and 0.23 Nm, respectively. The PWM frequency of the inverter was set to 15 kHz, and the bandwidth of the current controller was set to 400 Hz using the pole-zero cancellation technique presented in [19]. A film capacitor, with a capacitance of 10 uF, was used for the DC-link capacitor.

The gains of the speed controller, the block diagram of which is shown in Fig. 3, were tuned through several

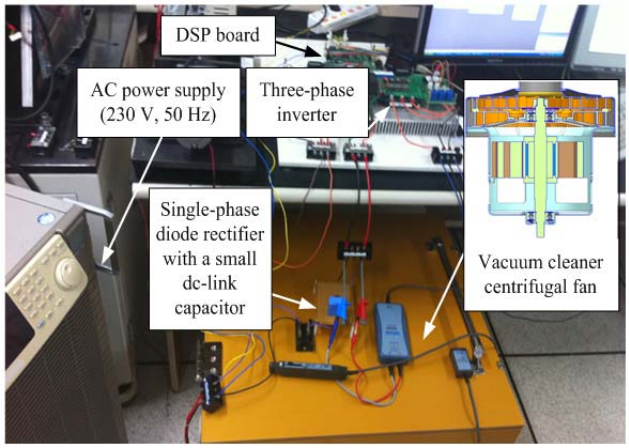

Fig. 10. The experimental setup.

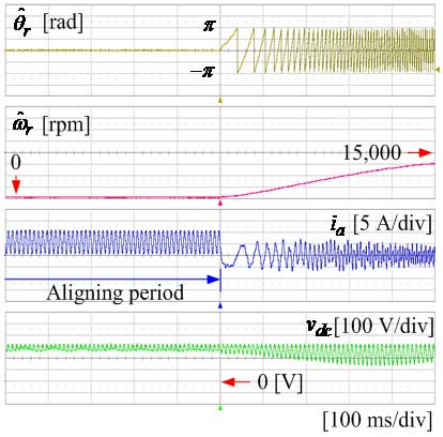

Fig. 11. Experimental result for the starting of PMSM.

experiments conducted. Fig. 3 shows that the proportional and integral gains of the first PI controller were set to 0.1 and 0.3, respectively; those of the second PI controller, in charge of outputting *q*-axis current reference, were set to 0.002 and 0.5, respectively. The bandwidth of the back-EMF estimator ω_{est} was set to 628 rad/sec; and ζ and ω_n, used for the notch filter in the proposed back-EMF estimator, were set to 0.7 and 628 rad/sec, respectively. Considering the high-speed operation, the time delay caused by the digital implementation of the controller should be compensated by the reliable operation of the current controller and the back-EMF estimator. This study utilized the method presented in [21].

The align and go method was utilized to commence PMSM. For this purpose, the first PI controller shown in Fig. 3 temporarily outputs a constant value to align the PMSM rotor to a specific direction. Fig. 11 shows that after alignment, PMSM is started using the estimated speed and position of the rotor. Fig. 11 also illustrates that the phase current i_a contains ripples, the frequency of which is 100 Hz, during the alignment period. Fig. 3 shows that this result is due to the structure of the speed controller, wherein the output of the first PI controller is multiplied by $\sin^2\theta_{grid}$.

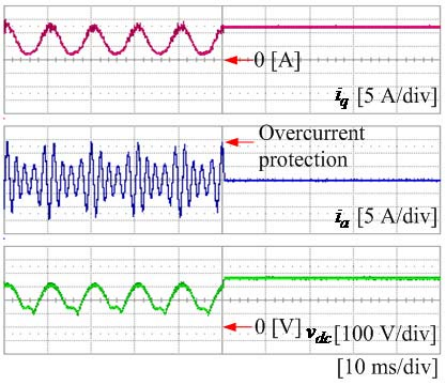

Fig. 12. Experimental result involving the conventional back-EMF estimator.

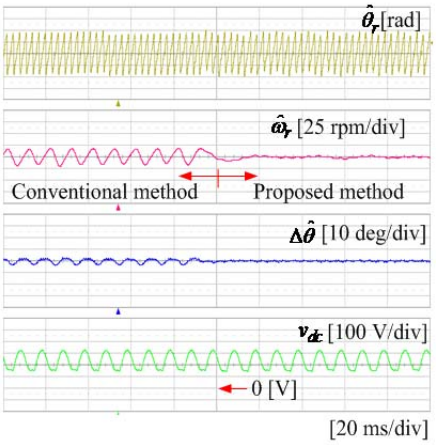

Fig. 13. Comparison of the estimated speed and position errors between the conventional and the proposed back-EMF estimator at 20,000 rpm.

Fig. 12 shows the experimental result of the high-speed sensorless control of PMSM, driven by a single-phase diode rectifier fed inverter with a small DC-link capacitor, with the conventional back-EMF estimator shown in Fig. 5 and the speed controller shown in Fig. 3. Fig. 12 shows that the over-current protection is triggered during the operation. The speed at the over-current protection point is approximately 29,000 rpm, although a maximum speed of 30,000 rpm is required for the vacuum cleaner used in this study. The cause of the excessive phase current in Fig. 12, which results in over-current protection, is the inordinate estimated position error in the sensorless control.

As described in Section III, the estimated position error in the sensorless control of PMSM at high-speeds mainly depends on $\Delta L_q i_\delta$. For this type of application, where a small DC-link capacitor is used and the PFC control is achieved by controlling the inverter output power without an additional hardware, ΔL_q is inevitable and cannot be easily compensated by using the online parameter estimation strategy. Figure 13 depicts the experimental comparison result between the conventional and the proposed back-EMF estimators at 20,000 rpm. Fig. 13 also illustrates that the conventional back-EMF estimator produces ripples in the estimated speed and position errors, resulting in a performance degradation in the high-speed sensorless control of PMSM. By contrast, the proposed back-EMF estimator successfully removes the ripples.

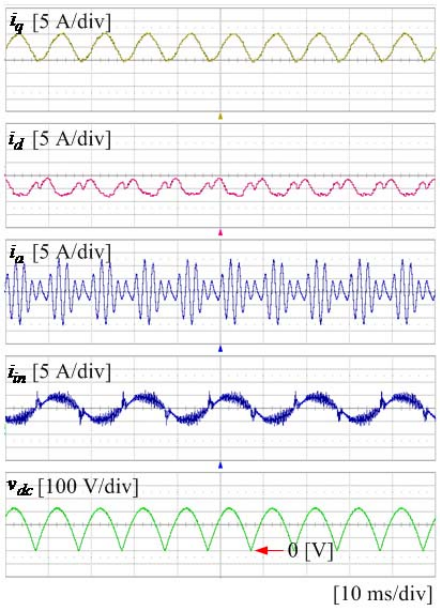

(a)

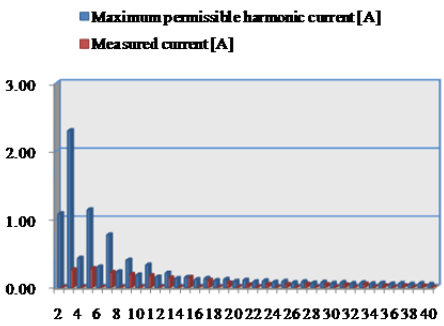

(b)

Fig. 14. (a) Experimental result with the proposed back-EMF estimator at 30,000 rpm. (b) Measured harmonic input current.

Fig. 14 shows the experimental result with the proposed back-EMF estimator at 30,000 rpm, which is the required maximum speed of the vacuum cleaner centrifugal fan used in this study. Fig. 14(a) presents that the *d*-axis current fluctuates with a frequency that is twice that of the AC mains voltage because the *d*-axis current reference is given by (5) to operate PMSM under a voltage constraint condition. The flux-weakening control is essential to operate PMSM at high-speeds under the voltage constraint condition; the *d*-axis current reference is often set to a negative value, and the magnitude of the *d*-axis current command increases as the motor speed increases [19]. The gains (k_1 and k_2) for the *d*-axis current reference generation should be prudently selected to satisfy both the flux weakening and the PFC control purposes. In the experiments, k_1 and k_2 were set to

0.002 and 0.0011, respectively; thus, modifying these gains based on a large variation in machine parameters is necessary. Fig. 14(a) shows that the current waveform at the AC mains is not perfectly sinusoidal because of the improper gain tuning in generating the *d*-axis current reference. However, Fig. 14(b) shows that the measured harmonic current at the AC mains satisfies the regulation of IEC 61000-3-2 (class A) [2]. The performance of input current waveform shaping can be improved by utilizing the method presented in [6]. However, the effect of the performance of the input current waveform shaping on the sensorless control is insignificant if the harmonic current at the AC mains is regulated within the limit of IEC 61000-3-2 (class A).

V. CONCLUSION

This study proposed the compensation method of periodic magnetic saturation effects for the high-speed sensorless control of PMSM driven by inverter output power control-based PFC strategy. In this strategy, a single-phase diode rectifier-fed inverter with a small DC-link capacitor is employed without any PFC circuits; the *d-q* axes inductances vary with twice the frequency of the AC mains caused by the specific inverter output power control. The back-EMF estimator was designed in the rotating reference frame to easily separate the periodic magnetic saturation effects from the estimated back-EMFs. Based on the analysis, the estimated back-EMF error at high-speeds mainly depends on the *q*-axis inductance error. The estimated position error based on the *q*-axis inductance error was also derived and verified through simulations. The analysis also presented that a simple method, wherein a notch filter with the cut-off frequency set to have the same as twice the frequency of the AC mains added to the back-EMF estimator, was proposed to compensate for the effect of the periodic *q*-axis inductance error on the estimated position error. The proposed method was implemented in driving a vacuum cleaner centrifugal fan, wherein the maximum operating speed reaches 30,000 rpm. The effectiveness of the proposed method was verified through experiments.

ACKNOWLEDGMENT

This study was financially supported in part by Samsung Electronics Co., Ltd.

REFERENCES

[1] K.-W. Lee, J. Hong, S. B. Lee, and S. Lee, "Quality assurance testing for magnetization quality assessment of BLDC motors used in compressors," *IEEE Trans. Ind. Appl*., Vol. 46, No. 6, pp. 2452–2458, Nov./Dec. 2010.

[2] Limits for harmonic current emissions (equipment input current ≤ 16 A per phase). IEC 61000-3-2, Part 3-2, 3rd ed., Nov. 2005.

[3] H.-S. Jung, S.-J. Chee, S.-K. Sul, Y.-J. Park, H.-S. Park, and W.-K. Kim, "Control of three phase inverter for AC motor drive with small dc-link capacitor fed by single phase AC source," in *IEEE 2012 Energy Conversion Congress and Expo (ECCE)*, pp. 2985-2991, 2012.

[4] K. Inazuma, H. Utsugi, K. Ohishi, and H. Haga, "High-power factor single-phase diode rectifier driven by repetitively controlled IPM motor," *IEEE Trans. Ind. Electron.*, Vol. 60, No. 10, pp. 4427-4437, Oct. 2013.

[5] W.-J. Lee, Y. Son, and J.-I. Ha, "Single-phase active power filtering method using diode-rectifier-fed motor drive," in *IEEE 2013 Energy Conversion Congress and Expo(ECCE)*, pp. 2461-2465, 2013 .

[6] Y. Son and J.-I. Ha, "Direct power control of three phase inverter for grid input current shaping of single phase diode rectifier with small DC link capacitor," *IEEE Trans. Power Electron.*, to be published, available online. DOI: 10.1109/TPEL.2014.2345421.

[7] K.-W. Lee, S. Park, and S. Jung, "A seamless transition control of sensorless PMSM compressor drives for improving efficiency based on a dual-mode operation," *IEEE Trans. Power Electron*., Vol. 30. No. 3, pp. 1446-1456. Mar. 2015.

[8] Z. Chen, M. Tomita, S. Ichikawa, S. Doki, and S. Okuma, "Sensorless control of interior permanent magnet synchronous motor by estimation of an extended electromotive force," in *Conf. Rec. IEEE-IAS Annu. Meeting*, Vol. 3, pp. 1814-1819, 2000.

[9] S. Morimoto, K. Kawamoto, M. Sanada, and Y. Takeda, "Sensorless control strategy for salient-pole PMSM based on extended EMF in rotating reference frame," *IEEE Trans. Ind. Appl.*, Vol. 38, No. 4, pp. 1054-1061, Jul./Aug. 2002.

[10] H. Kim, M. C. Harke, and R. D. Lorenz, "Sensorless control of interior permanent-magnet machine drives with zero-phase lag position estimation," *IEEE Trans. Ind. Appl.*, Vol. 39, No. 6, pp. 1726-1733, Nov./Dec. 2003.

[11] J. Kim, I. Jeong, K. Nam, J. Yang, and T. Hwang, "Sensorless control of PMSM in a ultra high speed region taking iron loss into account," in *IEEE 2014 Energy Conversion Congress and Expo(ECCE)*, pp. 2469-2476, 2014.

[12] Y. Lee and J.-I. Ha, "Sensorless drive for mono inverter dual parallel surface mounted permanent magnet synchronous motor drive system," *Transactions of Korean Institute of Power Electronics(KIPE)*, Vol. 20, No. 1, pp. 38-44, Feb. 2015.

[13] J.-J. Moon, H.-J. Heo, and J.-M. Kim, "Sensorless control of BLDC motor using d-q synchronously rotating reference frame concept," *Transactions of Korean Institute of Power Electronics(KIPE)*, Vol. 20, No. 3, pp. 232-238, Jun. 2015.

[14] I. Boldea, M. C. Paicu, G.-D. Andreescu, and F. Blaabjerg, ""Active flux" DTFC-SVM sensorless control of IPMSM," *IEEE Trans. Energy Convers*., Vol. 24, No. 2, pp. 314-322, Jun. 2009.

[15] Y. Inoue, K. Yamada, S. Morimoto, and M. Sanada, "Effectiveness of voltage error compensation and parameter identification for model based sensorless control of IPMSM," *IEEE Trans. Ind. Appl.*, Vol. 45, No. 1, pp. 213-221, Jan./Feb. 2009.

[16] S. Ichikawa, M. Tomita, S. Doki, and S. Okuma, "Sensorless control of synchronous reluctance motors based on extended EMF models considering magnetic

saturation with online parameter identification," *IEEE Trans. Ind. Appl.*, Vol. 42, No. 5, pp. 1264-1274, Sep./Oct. 2006.
[17] K.-W. Lee and J.-I. Ha, "Evaluation of back-EMF estimators for sensorless control of permanent magnet synchronous motors," *Journal of Power Electronics*, Vol. 12, No. 4, pp. 604-614, Jul. 2012.
[18] K.-W. Lee, "High-speed sensorless control of a PMSM operating under periodic magnetic saturation conditions," *in IEEE 2014 Energy Conversion Congress and Expo(ECCE)*, pp. 4478-4483, 2014.
[19] S.-K. Sul, *Control of Electric Machine Drive Systems*, John Wiley & Sons, 2011.
[20] J. Hong, D. Hyun, S. B. Lee, J. Yoo, and K. Lee, "Automated monitoring of magnet quality for permanent magnet synchronous motors at standstill," *IEEE Trans. Ind. Appl.*, Vol. 46, No. 4, pp. 1397-1405, Jul./Aug. 2010.
[21] B.-H. Bae and S.-K. Sul, "A compensation method for time delay of full digital synchronous frame current regulator of PWM AC drives," *IEEE Trans. Ind. Appl.*, Vol. 39, No. 3, pp. 802-810, May/Jun. 2003.

Kwang-Woon Lee was born in Seoul, South Korea. He received the B.S., M.S., and Ph.D. degrees in Electrical Engineering from Korea University, Seoul, Korea, in 1993, 1995, and 1999, respectively. From 2000 to 2002, he was with Samsung Advanced Institute of Technology, Yongin, Korea, where he worked on the development of micro-electromechanical system sensor applications. From 2002 to 2007, he was a senior research engineer at the Samsung Living Appliance R&D Center, Samsung Electronics, Suwon, Korea, where he was engaged in research on sensorless motor drive systems for refrigerators and air conditioners. He is currently an associate professor in the Department of Electronic Engineering, Mokpo National Maritime University Mokpo, Korea. His current research interests include power electronics and control, which include AC machine drives, digital signal processing-based control applications, and fault diagnosis of electrical machines.